RESEARCH ARTICLE | JUNE 17 2025

Tuning the crystallinity of TiO_2 coatings synthesized by an atmospheric pressure dielectric barrier discharge in a single step process FREE

Special Collection: Papers from the AVS 70th International Symposium

Nicolas Fosseur; Thomas Fontaine; David Petitjean; Loïc Malet; Rony Snyders; Stéphane Godet; François Reniers

+ Author & Article Information

J. Vac. Sci. Technol. A 43, 043413 (2025)

https://doi.org/10.1116/6.0004617 **Article history**

Titanium dioxide in its anatase form is of significant interest nowadays due to numerous properties such as biocompatibility, photoactivity under ultraviolet irradiation, or corrosion resistance. In this paper, titanium dioxide (TiO_2) films are synthesized with a controlled substrate temperature going up to 673 K. Crystalline anatase was synthesized in a low power atmospheric pressure dielectric barrier discharge in a single step process. The effect of deposition parameters (plasma gas, the voltage input, precursor flow, deposition time, and substrate temperature) on the crystal size, crystallinity, and coating morphology was studied. It shows that the crystal size can be tuned, that the layers can have a transition from hydrophilicity to hydrophobicity, and that the coating morphology can be modified by optimizing these parameters. Finally, it is found that crystalline anatase TiO_2 can be grown at a substrate temperature as low as 523 K in an atmospheric pressure plasma enhanced chemical vapor deposition process.

Topics

Atmospheric processes, Crystal structure, Scanning electron microscopy, X-ray diffraction, Chemical vapor

deposition, Crystallization, Hydrophobic effect, Plasma applications

I. INTRODUCTION

Titanium dioxide (TiO_2) is used in various fields such as biomedical applications due to its biocompatibility,[1] lithium-ion batteries[2] or as photoactive material for depollution,[3,4] CO_2 reduction,[5] or H_2 production.[6] It exhibits a wide range of properties of significant interest nowadays such as a transition from hydrophobicity to hydrophilicity depending on the microstructure[7] or the chemical composition with carbon (methyl) contamination,[8] its biocompatibility,[9] or even good corrosion resistance.[10] TiO_2 can be synthesized by various techniques such as wet processes (sol-gel,[5,11] hydrolysis[12,13]) or dry processes such as physical vapor deposition[14] or plasma enhanced chemical vapor deposition (PECVD).[15,16] Historically, these dry processes have been realized at low pressure and it allows a fine-tuning of the incoming particle energy, a good control of the growth mode, and limits contamination.[14] However, the associated pumping costs represent a considerable part of the electrical consumption of the facility.[17] Nowadays, there is a growing interest in investigating more sustainable processes with lower electrical consumption. In this context, many researchers are currently investigating deposition processes that operate at atmospheric pressure.[18] This generates new challenges including control of the growth mode, of the crystallization process, or of the purity of the deposited film.

Titanium tetraisopropoxide (TTIP) is often chosen as a precursor as it prevents the release of toxic by-products, contrary to titanium tetrachloride ($TiCl_4$) for instance, even though the latter one is known to give reliable results in anatase crystallization with variable substrate temperature.[19]

Atmospheric plasma deposition of TiO_2 has been the focus of

recent investigations, and a review can be found in the article of Banerjee *et al.*[20] For instance, Collette *et al.* deposited TiO_2 using a radiofrequency plasma torch,[21] Baba *et al.*[22] deposited TiO_2 with selective facets with controlled deposition parameters using microwave atmospheric pressure (AP)-PECVD plasma discharge, Homola *et al.*[23] used a diffuse coplanar discharge to deposit TiO_2, other researchers used a combined process of atmospheric pressure plasma jet and chemical vapor deposition to deposit titanium dioxide.[24–26] Chen *et al.* were among the first ones to deposit TiO_2 using an atmospheric pressure dielectric barrier discharge (AP-DBD) system.[27] However, a postdeposition annealing step (at 673 K) was still required to crystallize TiO_2 in the anatase phase. Even when other authors evaluated a one-step deposition, they only managed to obtain amorphous TiO_2 films.[27–29] Remy *et al.*[30] combined a DBD with a substrate inductive heating system to obtain, in one step, crystalline TiO_2 at atmospheric pressure. However, no parametric study of the factors influencing crystallization was performed for TiO_2, only a few have reported the effects of AP-DBD plasma parameters in the case of crystalline V_2O_5 localized deposition[31,32] and provide insight into TiO_2 crystallization tuning in an AP-DBD.

TiO_2 anatase is known for its photocatalytic properties under UV light. According to the literature, an optimal crystal size is estimated to be around 20–25 nm.[33,34] The main objective of the present work is to establish a methodology for tuning the crystal size when the material is deposited by a low power DBD. Another objective is to lower the substrate temperature during deposition, since for all its applications, as it is challenging[35,36] to broaden the range of materials on which this inorganic coating can be deposited. In fact, Wang *et al.*[35] could not deposit crystalline TiO_2 below 723 K (450 °C) as a substrate temperature, whereas Youssef *et al.*[36] could not deposit crystalline coatings below 623 K (350 °C), both using low pressure processes. It is challenging to crystallize the layer in atmospheric pressure processes below

crystallize the layer in atmospheric pressure processes below this temperature. However, using low pressure PECVD, Borras *et al.*[15,37] have established a lower limit of crystallization temperature of 523 K (250 °C).

II. MATERIALS AND METHODS

A. Materials

TTIP 97% from Sigma-Aldrich (CAS number: 546-68-9, product number: 205273) is used as a precursor. It was chosen for its limited toxicity and hazardous properties and for its high vapor pressure. The substrates used for the study are silicon wafers (n-doped faced {100}) provided by Pi-kem. Oxygen (Air Liquide, Alphagaz 1, P0361) is used as a reactive gas, and argon Ar (Air Liquide, Alphagaz 1, P0021) and nitrogen (N_2; Air Liquide, Alphagaz 1, P0271) are used as main plasma gases.

B. Experimental setup

The setup used to deposit the layers of interest in this study is a home-built DBD described in Fig. 1. It consists of a cylindrical reactor supplied with different gases, a pumping module to clean the reactor atmosphere, and a heating module to control the substrate temperature.

FIG. 1.

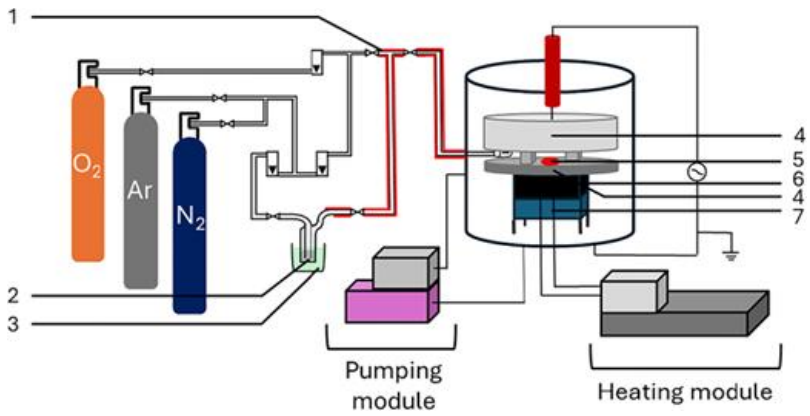

Experimental setup; (1) heated pipe, (2) bubbler filled with

the titanium precursor, (3) oil bath, (4) dielectric with the electrode inside, (5) susceptor (nickel plate), (6) ferrite induction coil, and (7) fan. Additionally, there are pumping and heating modules as described in Remy *et al.* patent (Ref. 38).

Either argon or nitrogen is the main plasma and carrier gas of this study and a fraction (15%) of the total flow passes through the bubbler to carry the vaporized titanium precursor [$Ti(OC_3H_7)_4$, TTIP; see **Fig. 2**]. The inert gas fraction passing in the bubbler is abusively named TTIP flow in the remainder of the present work. Oxygen is used as a reactive gas (15% of the total flow).

FIG. 2.

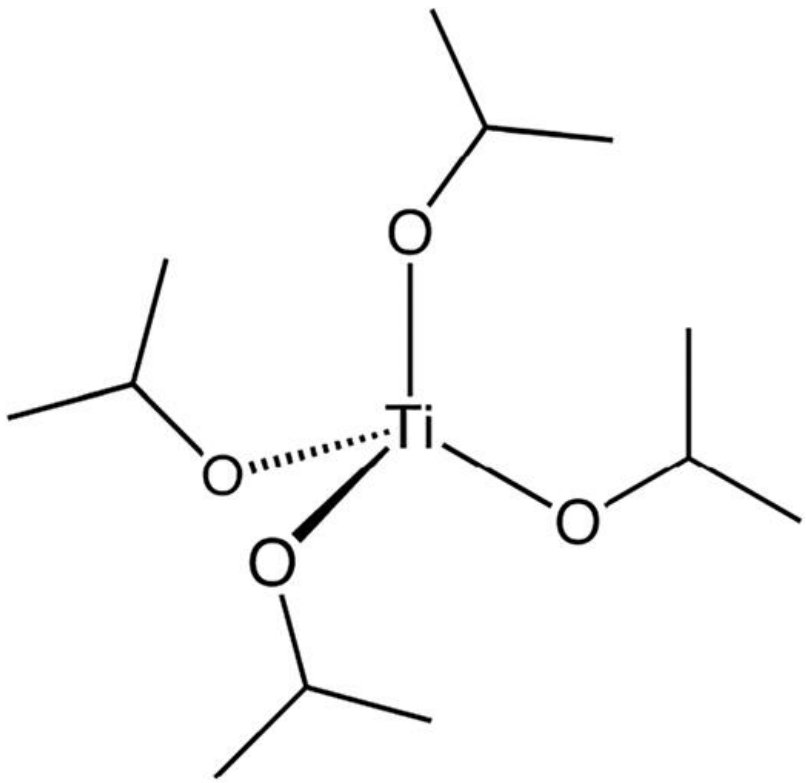

Titanium tetraisopropoxide (TTIP).

To prevent precursor condensation, the pipes are heated at a temperature of at least 15 °C above the bubbler temperature with a minimum of 90 °C (363 K). The reactor is a glass cylinder with an outer diameter of 21.4 cm, a thickness of 0.8 cm, and a height

of 18.3 cm. The reactor presented in Fig. 1 contains eight different apertures to connect the pipe arrival, the pressure gauge, the electrical wires, and the gas inlet and outlet. It also allows spectroscopic or mass spectrometric studies when needed.

The anode is located inside the reactor, 3 mm below the gas inlet. It consists of a 10 cm diameter stainless steel mesh on top of which there is a 3 mm thick and 14 cm diameter mica layer as a dielectric material. In its center, there is a nickel plate on which the substrate is glued to be heated thanks to the induction coil which is located below the anode and cooled by a fan (7 in Fig. 1).

Two pieces of 3 mm thick and 2 cm^2 area glass sheets are placed on top of the mica dielectric to provide an adequate gap between the two dielectrics. The top electrode is a copper disk and is inserted and sealed in an alumina crucible (8.2 cm in diameter and 3.9 mm thick).

The pumping module has two primary functions. First, it is required to empty the chamber prior to deposition. Second, it helps in filling the reactor with the plasma reaction medium. The chamber is pumped down to a pressure of less than 9 Torr and then backfilled with argon. This procedure is repeated twice to prevent contamination from the atmosphere. The heating induction system is a homemade patented system[38] that allows the substrate temperature to be tuned from 20 °C (ambient temperature) to 500 °C.

The power is injected into the system in two modes: continuous AC [see Fig. 3(a)] and pulsed AC, sometimes referred to as "burst" mode [Fig. 3(b)]. The burst mode is characterized by the time during which voltage is applied (Time ON = T_{ON}) and not applied (Time OFF = T_{OFF}), which are used to calculate the duty cycle (DC). DC is defined as the ratio between T_{ON} and the sum

of T_{ON} and T_{OFF} [Eq. (1)]. The duty cycle varies but the total duration of $T_{ON} + T_{OFF}$ equals 1 ms. The power generator is an AFS G10S-V instrument operating at 2.7 kHz. Table I shows the operating conditions used for the present research,

$$DC = \frac{T_{\mathrm{ON}}}{T_{\mathrm{ON}} + T_{\mathrm{OFF}}}. \quad (1)$$

FIG. 3.

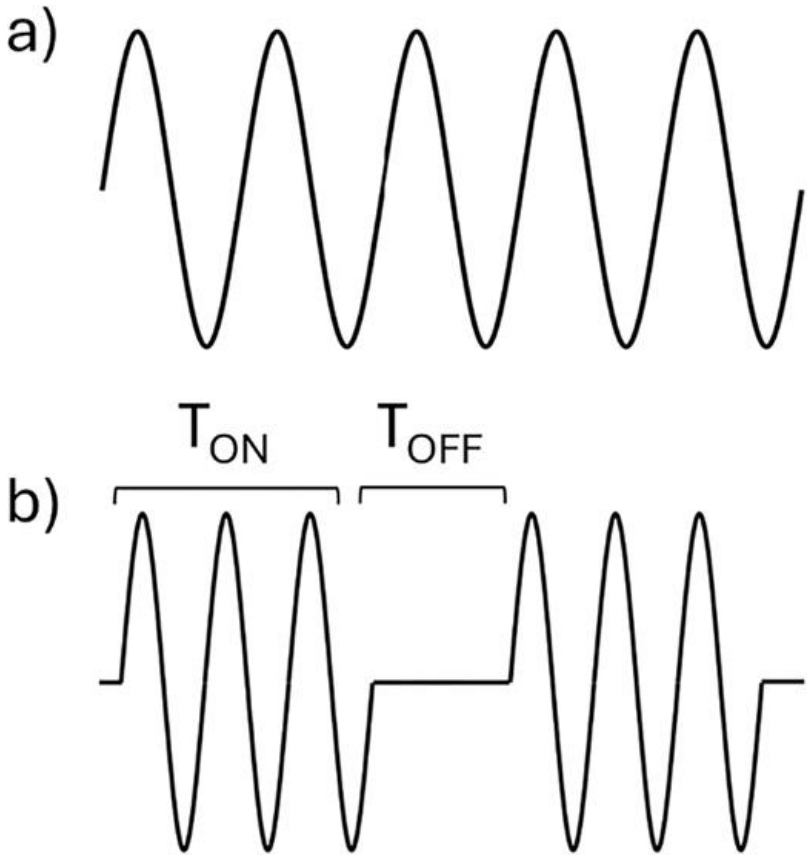

Distinct types of input signals (a) continuous AC and (b) pulsed AC or burst.

TABLE I.

Table gathering the different deposition parameters and some of their variations along the present study.

	Default parameters	**Variations**

Substrate	Si wafer {100}	
Frequency (kHz)	2.7	
Mean applied power (W)	45	
Gap (mm)	3	
Carrier gas	Ar	Ar, N_2
Input signal (time ON/time OFF)	Continuous	Continuous, pulsed 0.2 ms ON/0.8 ms OFF, pulsed 0.5 ms ON/0.5 ms OFF
Deposition time (min)	20	5, 10, 20, 30
Bubbler temperature (K)	333	303, 313, 323, 333, 343, 353, 363
Substrate temperature (K)	673	473, 523, 573, 623, 673
Total flow (slm)	10	
O_2 flow (slm)	1.5	
TTIP flow (slm)	1.5	

The reaction occurring in PECVD is complex. Equation (2) is proposed as a global reaction mechanism occurring when TTIP is injected into an Ar–O_2 plasma for TiO_2 deposition:[30]

$$\mathrm{Ti\,(OC_3H_7)_4 + 36O \rightarrow Ti\,O_2 + H_2O + CO_2,} \tag{2}$$

where atomic oxygen comes from the dissociation of O_2 in the plasma mostly following Eqs. (3) and (4):

$$\mathrm{O_2 + e^- \rightarrow O_2^+ + 2e^-,} \tag{3}$$

$$\mathrm{O_2^+ + e^- \rightarrow 2O.} \tag{4}$$

Other researchers suggest that the electrons present in the

plasma degrade directly the TTIP by breaking the O–C bond, most likely once, or even twice to release one or two isopropyl groups and resulting in carbonated TiO_2 [Eqs. (5) and (6)]. They actually never observed full fragmentation due solely to the electrons,

$$\mathrm{Ti\,(OC_3H_7)_4 + e^- \rightarrow Ti\,(OC_3H_7)_3O^- + C_3H_7^+ + e^-,} \tag{5}$$

$$\mathrm{Ti\,(OC_3H_7)_4 + e^- \rightarrow Ti(OC_3H_7)(OC_3H_6)O^{2-} + 2C_3H_7^+ + H^+ + e^-.} \tag{6}$$

Different phenomena then may occur during the heated PECVD of TTIP into TiO_2 such as the hydrolysis of TTIP,[39]

$$\mathrm{Ti\,(OC_3H_7)_4 + 2\,H_2O \rightarrow Ti\,O_2 + 4C_3H_7\,OH,} \tag{7}$$

where water is produced by the degradation of TTIP in Eq. (2). Thermal decomposition of TTIP [Eqs. (8) and (9)] may also occur in the close vicinity of the heated substrate,[40]

$$\mathrm{Ti\,(OC_3H_7)_4 \overset{T>673\ K}{\longrightarrow} Ti\,O_2 + 4C_3H_6 + 2H_2O,} \tag{8}$$

$$\mathrm{Ti\,(OC_3H_7)_4 \overset{T<673\ K}{\longrightarrow} Ti\,O_2 + 2C_3H_6 + 2C_3H_7\,OH.} \tag{9}$$

C. Film deposition

Unless stated otherwise, films are deposited with the “default conditions” listed in Table I. The parametric study includes variation in the substrate temperature, the deposition time, the precursor flow (through the bubbler temperature), the nature of the plasma gas, and the power injection mode. The range of variations for each parameter is listed in Table I. The default parameters presented in Table I were either determined by previous work[28,29] or optimized prior to any further work.

In this study, different temperatures are used and controlled in

In this study, different temperatures are used and controlled in different ways. The temperature of the liquid precursor is controlled by immersing the bubbler in a stirred (400 rpm) oil bath as presented in Fig. 1 (number 3) and measured by a thermometer immersing without contact at the level of the bottom of the bubbler. The temperature of the heated pipe is measured with a Chromel-Alumel thermocouple (K type) with an accuracy of 10 K. The temperature of the substrate is also measured with this thermocouple in a quasi-closed system and with the same gas flow as for film depositions.

D. Characterization techniques

The crystallinity of the deposited anatase coatings was analyzed using a D8 Advance Eco Brüker x-ray diffractometer with a Cu k_α ($\lambda = 1.5418$ Å) anode. The mean crystal size can be calculated from the diffraction spectra using the Scherrer equation [Eq. (10)],

$$d = \frac{K\,\lambda}{\beta\cos(\theta)}, \tag{10}$$

where d is the mean crystal size (nm), K is a constant factor equal to 0.89 for TiO_2, λ is the wavelength of the source (nm), ϑ is the diffraction angle, and β is the full width at half maximum (FWMH in rad) of the main diffraction peak (here the {101} plane at 25.4° for anatase) and the β value can be corrected using the equation $\beta = \sqrt{H^2 - s^2}$, where H is the total full width at half maximum (rad) and s is the instrumental broadening (rad; typically 0.05 rad).

Chemical surface characterization was performed with a physical electronics PHI—VersaProbe II system operating with a monochromatic Al K_α x-ray source (1486.6 eV). Full surveys were acquired between 0 and 1100 eV with a pass energy of 93.9 eV, a time per step of 20 ms, and three scans were averaged for one spectrum. To ensure a suitable atomic quantification, full surveys were measured at five distinct locations on each sample. Surface spectra and bulk spectra were acquired (the latter one after a 2

min sputtering with a 3 kV Ar beam). Surface composition of the deposited layer can be calculated using the formula in Eq. (11),

$$P_i = \frac{\frac{I_i}{S_i}}{\sum_{i=1}^{n} \frac{I_i}{S_i}}, \quad (11)$$

where P_i is the relative atomic concentration of the i element (at. %), I_i is the area of the peak of i element (measured by XPS), and S_i is the sensitivity factor of i.

A SU-70 Hitachi field emission gun scanning electron microscope (FEG-SEM) operated at 15 kV and 29 μA was used to analyze the surface morphology of the samples.

The plasma phase was studied using an Andor Shamrock 500i-D2 optical emission spectrometer (OES). The light intensity is measured by a sensor camera (iDU420A-OE). The parameters used for collecting measurements are depicted in Table II. Different gratings were available for the diffraction network, which are related to the resolution of the spectra. There were 1200, 1800, and 2400 lines per mm which, respectively, correspond to 0.06, 0.04, and 0.03 nm of spectral resolution (according to the spectrometer datasheet). The fitting required to estimate the gas temperature is done on high resolution spectra with the MASSIVEOES software.[41]

TABLE II.

Parameters of the OES experiments.

Measurement	Species of interest	Range (nm)	Grating (l/mm)	Exposure time (s)	Accumulation
Species identification	Full spectrum	200–900	1200	2	10
Rotational temperature	N_2 (C-B)	345–365	2400	20	10

Species identification	O	770–785	1200	20	10

Electrical parameters such as voltage and current are measured using a high voltage probe (Tektonix P6015A) and a current monitor (Pearson 6595). They are both connected to a digital oscilloscope (Tektronix DPO3032).

A Krüss DSA100 was used to perform water contact angle (WCA) measurements. A deionized water droplet of 3 μl was deposited on the sample with a flow of 409.3 μl/min. The WCA were evaluated using the *Drop shape analysis* software using the *tangent 1* method. To calculate the error in the measurement, each sample was assessed five times.

III. RESULTS AND DISCUSSIONS

Figure 4 shows that pure TiO_2 coating can be deposited by PECVD at atmospheric pressure using the default parameters (see Table I). The as-deposited layer contains carbon on its surface, due probably to unreacted residuals of TTIP and confirms what Bjarnason *et al.*[42] have studied finding that TiO_2 deposition starting with TTIP consistently contains 20 at. % of carbon at the surface. After surface removal by Ar sputtering, XPS reveals that less than 1 at. % carbon remains in the bulk of the deposited coating. This suggests that reaction (2) is complete.

FIG. 4.

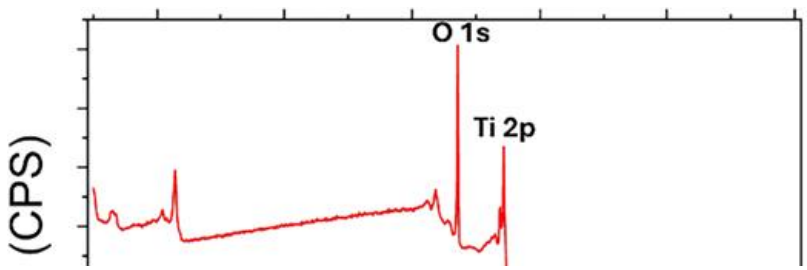

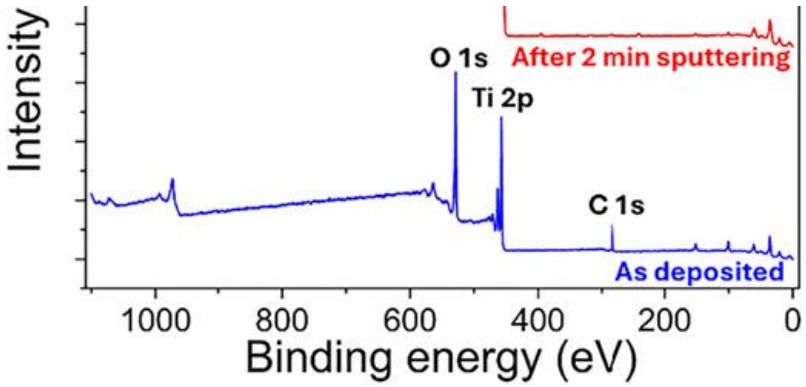

XPS spectra of an anatase coating deposited with the default parameters (see Table I) before and after 2 min of Ar sputtering.

A. Influence of the plasma gas

Although argon is the most commonly used inert gas for PECVD, it is sometimes substituted by nitrogen because the latter one is known to allow lower gas temperatures[43,44] that can affect film crystallization.

Figure 5 presents the diffraction peaks of a typically deposited layer with Ar (red) or in N_2 (in black). The same peaks are present, such as the {101} diffraction plane at 25.4° of anatase, the K_β of Si {100} at 32.9° and the small "bumps" at 38.1° ({004}), 48.2° ({200}) and 55° ({211}) are other less dominant diffraction peaks of TiO_2 anatase. The main change between the two spectra is the FWMH value of the diffraction peak at 25.4°. This change corresponds to, via the Scherrer equation, a change in the crystal size from 10.4 ± 0.05 nm for the deposition in Ar to 20.38 ± 1.16 nm for the deposition in N_2.

FIG. 5.

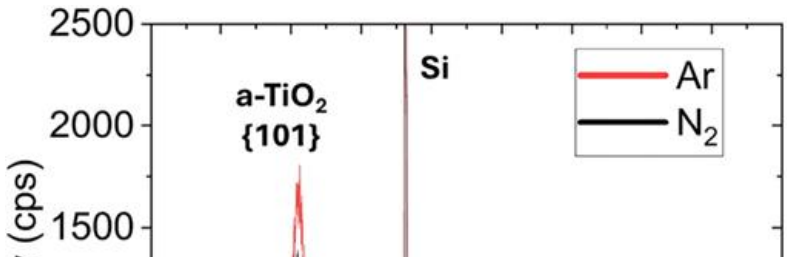

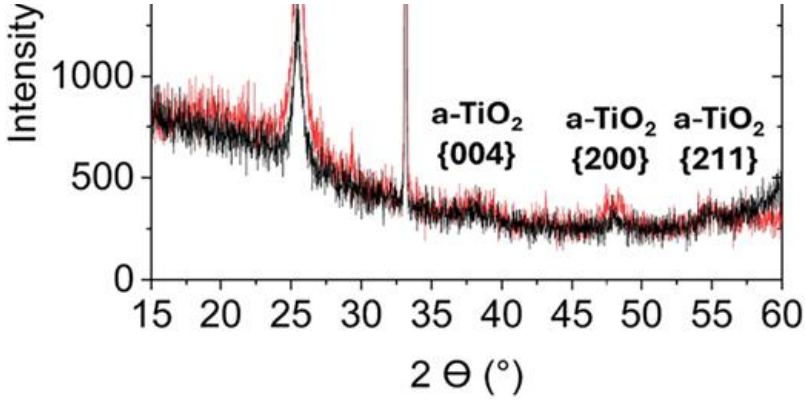

XRD of TiO_2 coatings deposited with Ar or N_2 as a carrier gas (a continuous power of 45 W, a substrate temperature of 673 K, a bubbler temperature of 333 K, and 20 min of deposition time).

SEM images presented in Fig. 6 show that the anatase TiO_2 deposited by atmospheric pressure PECVD forms a cauliflower-like structure. It can be seen from Figs. 6(a) and 6(b) that the structure is the same, but a densification of the layer as well as a reduction of the size of the cauliflower is observed when N_2 is used.

FIG. 6.

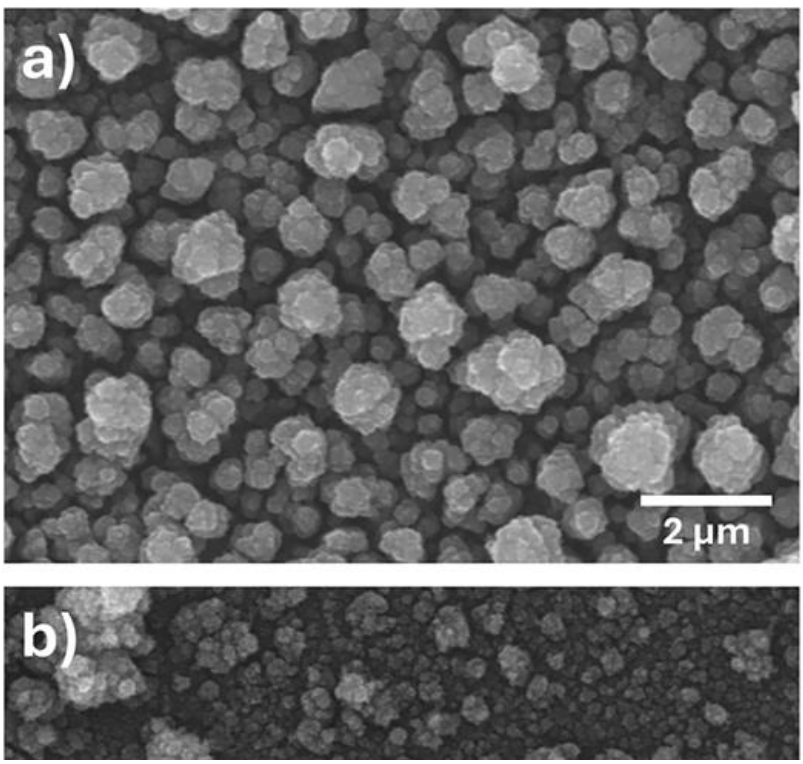

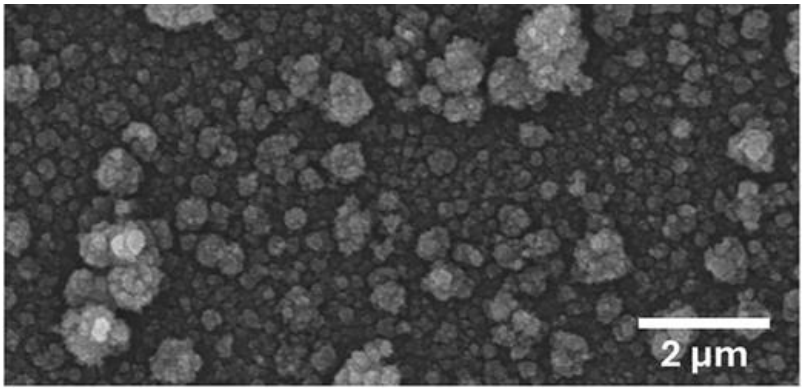

(a) SEM image of the reference sample deposited in an Ar atmosphere and (b) SEM image of the sample deposited in an N_2 atmosphere. Magnification x10 000 and scale bar = 2 μm.

Both changes (average crystal size and crystallinity) are caused by the changes in plasma properties. Indeed, it is well known that argon has a lower breakdown voltage than nitrogen and is more ionized than nitrogen in a low power discharge. The difference in the ionization density leads to an increase in the local electric field strength and then to an increase in the local gas temperature. Amini *et al.*[45] illustrated this principle by changing the crystal size and microstructure of a TiO_2 with a glow post-discharge with N_2 or Ar plasma gas. In the present work, the gas (rotational) temperature was measured by OES and plotted in Fig. 7.

FIG. 7.

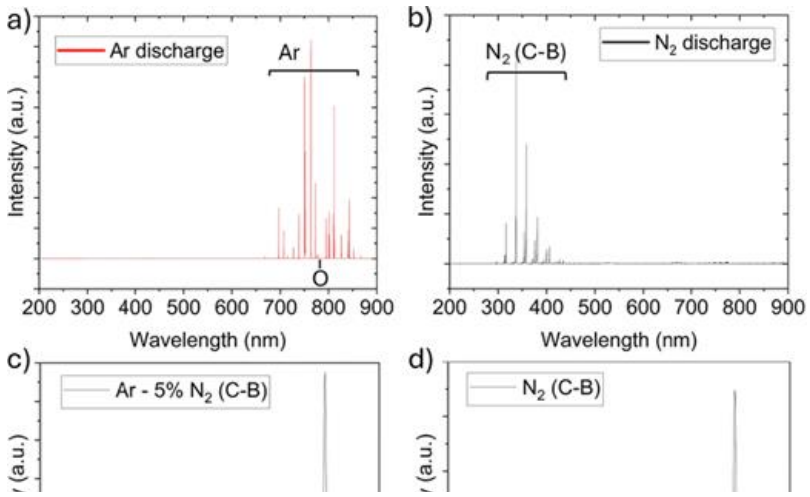

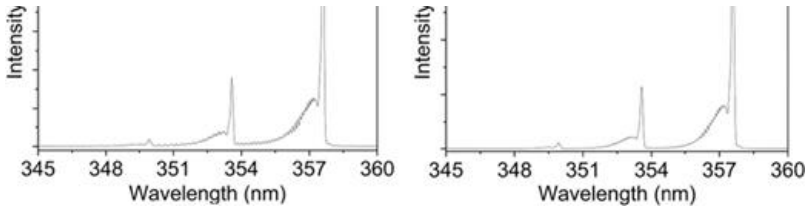

OES spectra of (a) full spectrum of a 70% Ar–15% O_2–15% TTIP discharge at 45 W and (b) full spectrum of a 70% N_2–15% O_2–15% TTIP discharge at 45 W. (c) High resolution spectra of N_2 (C–B) signal in Ar discharge with controlled content of nitrogen (65% Ar–5% N_2–15% O_2–15% TTIP) at 45 W. (d) High resolution spectra of N_2 (C–B) signal in N_2 discharge (70% N_2–15% O_2–15% TTIP) at 45 W.

Figures 7(a) and 7(b) represent full OES spectra of discharges consisting of 70% plasma gas (Ar or N_2)–15% O_2–15% TTIP. They show mostly the lines/bands of the plasma gas species (Ar or N_2) and low intensity emission lines of atomic oxygen (at 777 nm). The rotational temperature was determined on the N_2 C–B bands, with the help of the MASSIVEOES software.[41] For the Ar plasma, a small amount of N_2 (<5%) was added for that purpose. An average rotational temperature was estimated to be 433 ± 5 K (vibrational temperature = 3424 ± 29 K) for the argon discharge and 341.5 ± 1.5 K (vibrational temperature = 3186 ± 27 K) for the nitrogen discharge. The gas temperature is, therefore, higher in an argon discharge compared to a nitrogen discharge which agrees with the literature.[43,44] These OES temperature measurements were also performed with the substrate heating system and show an average increase in the rotational temperature of 100 ± 10 K for a surface heating at 673 K. This supports the possibility of the side reactions (8) and (9) for thermal decomposition of TTIP.

No significant bands of OH or CH bands were detected on the OES spectra, contrary to atomic oxygen line, presented in Fig. 8. Interestingly, a significant decrease in the atomic oxygen emission line was observed when TTIP was added to an Ar-O_2

discharge. This suggests that reaction (2) where atomic oxygen is involved in the synthesis of TiO_2 is a potential pathway.

FIG. 8.

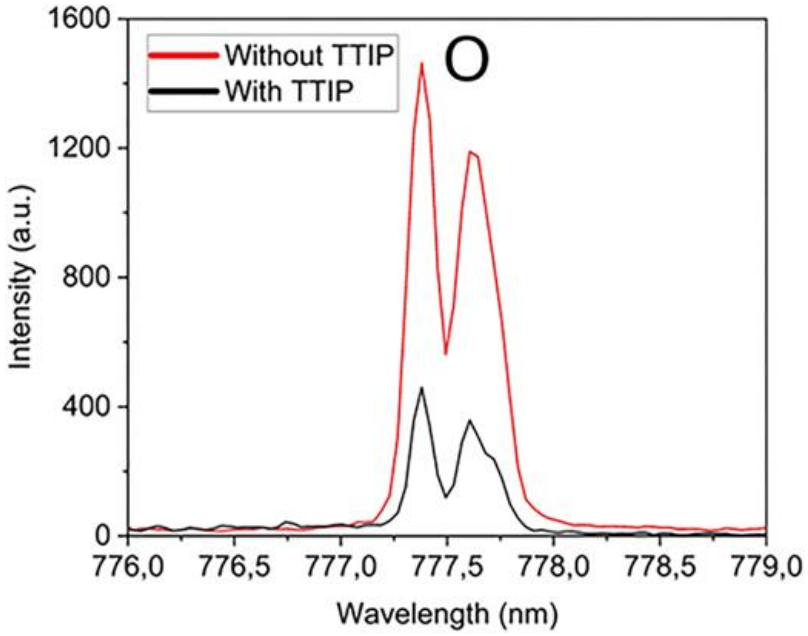

High resolution OES spectra in Ar–O_2 discharge of the atomic oxygen signal either containing TTIP (in black) or not (in red) in the range between 776 and 779 nm.

B. Voltage input

Pulsing the electrical input mostly results in an increase in the power during the “time ON,” while leaving the power at zero during the “time OFF.” Tuning the ON and OFF time at the same mean applied power, therefore, leads to much higher power during the lower ON time (as seen in Table III). Figure 9 presents the measured voltage and current curves for the different DBD modes.

FIG. 9.

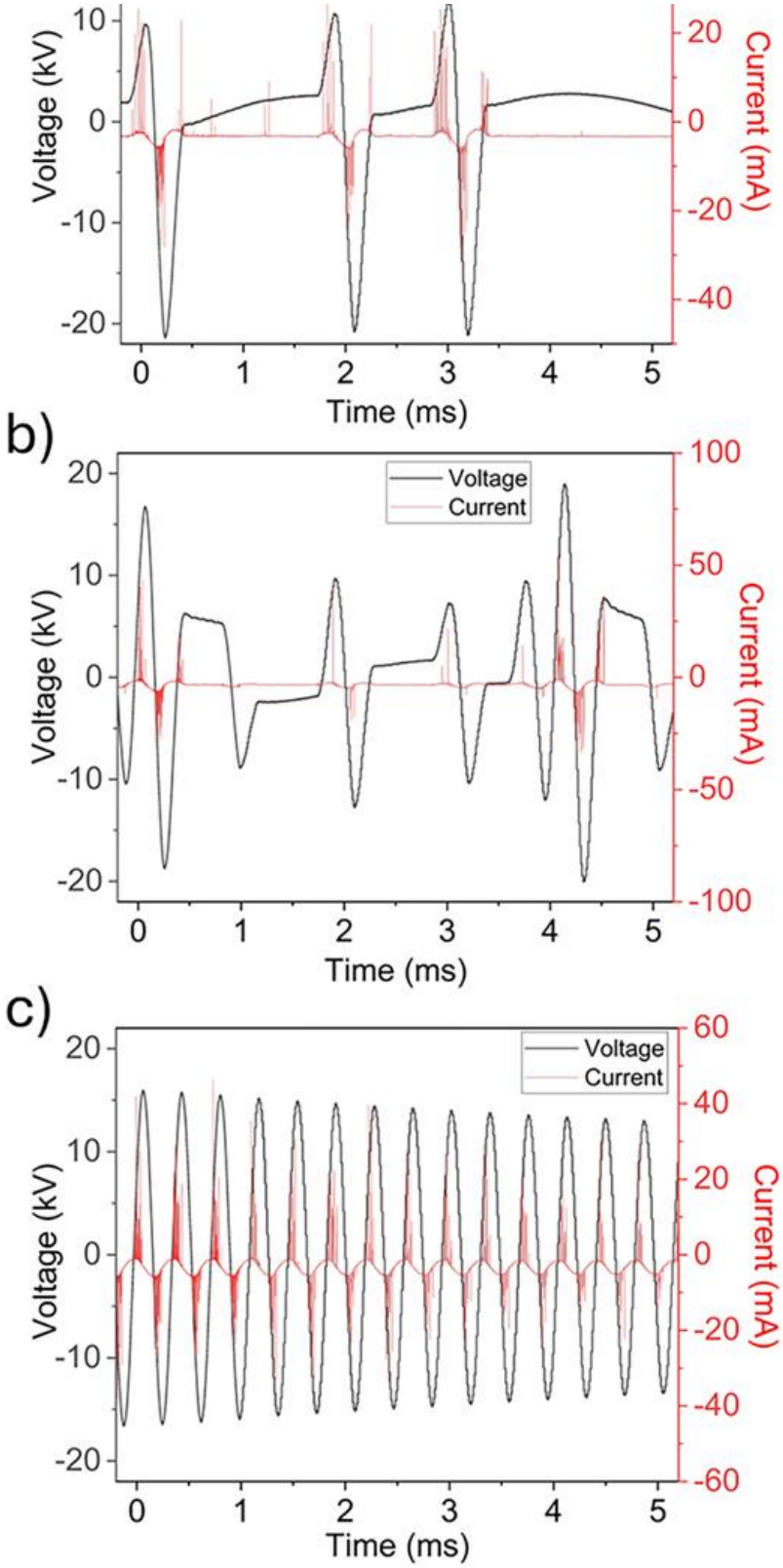

Voltage (black) and current (red) for the different DBD mode discharges. (a) Electrical measurement for a duty cycle of 20%, (b) electrical measurement of 50%, and (c) electrical measurements for a duty cycle of 100%.

TABLE III.

Conversion between mean applied power and instantaneous power for pulsed discharge.

Pulsing parameter	% of ON time of the plasma (duty cycle)	Mean applied power (W)	Power during time ON (W)
0.2/0.8	20	45	225
0.5/0.5	50	45	90
Continuous	100	45	45

Values of power during time ON of the plasma are calculated by dividing the mean applied power by the DC.

Figure 10 shows the XRD spectra of TiO_2 coatings deposited for various ON/OFF times. All coatings exhibit a mean crystal size of 12 ± 2 nm. Therefore, there is no change in crystal size as the power is pulsed. However, pulsing was shown to lead to significant improvement in the case of crystallizing vanadium oxide[32] deposited with atmospheric pressure DBD plasma.

FIG. 10.

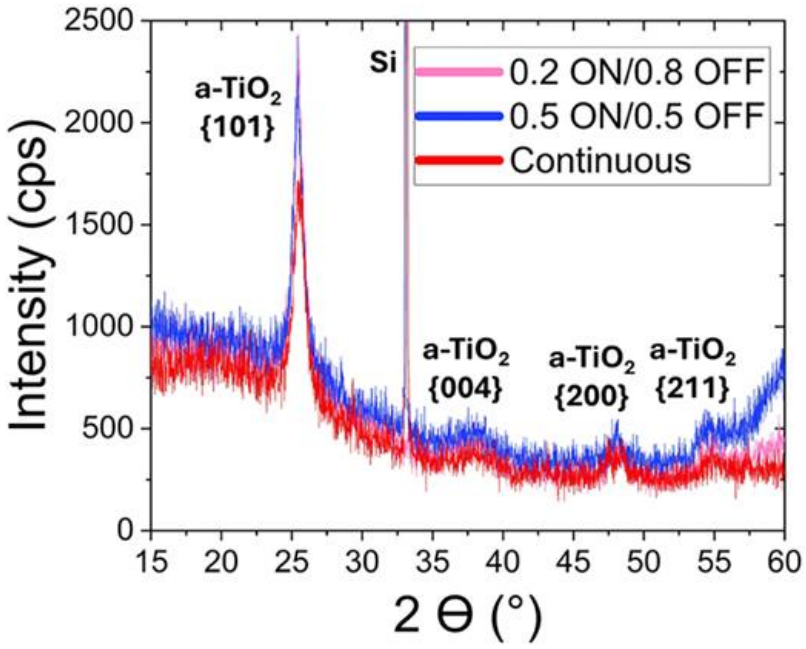

XRD spectra of the different voltage inputs with a mean applied power of 45 W for 20 min with a substrate temperature of 673 K and a bubbler temperature of 333 K with Ar as a carrier gas.

As the peak intensity increases for a short ON time, there is an increase in the overall crystallinity of the coating. The pulsed electrical input leads to a change in the surface chemical composition of the coating and to the resulting hydrophilic behavior of the surface, as shown in Fig. 11.

FIG. 11.

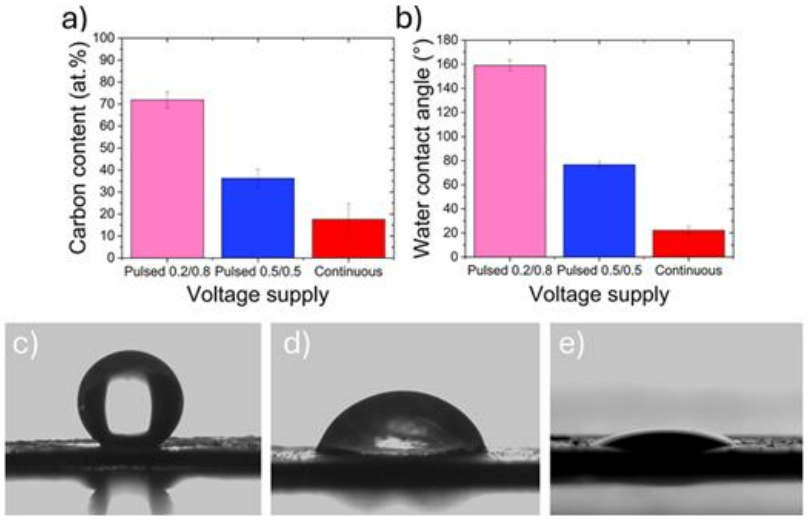

(a) Evolution of the surface carbon content (measured by XPS) depending on the voltage input. (b) Evolution of the WCA as a function of the voltage supply. (c) WCA image of a water droplet on the surface deposited with a pulsed signal 0.2/0.8. (d) WCA image of the droplet on the surface deposited with a pulsed signal 0.5/0.5. (e) WCA image of the droplet on the surface deposited with a continuous AC signal.

For short ON time (short duty cycle), namely, at very high instantaneous power (see Table III), coatings exhibit a high carbon content (C at. %; measured by XPS) at the surface of the layer and are very hydrophobic. In the continuous mode, the coatings have a low carbon content and are hydrophilic. Banerjee

et al.[20] discussed the observation of Mathur and Kuhn[46] that increasing plasma power leads to an increased carbon content for TiO_2 deposition with carbonaceous titanium precursor. In Fig. 11(b), the WCA of the layer follows the same trend as the one presented in Fig. 11(a), meaning a decreasing WCA with an increasing time ON of the plasma (increasing duty cycle). There is a clear switch from hydrophobicity to hydrophilicity going from 160° to 20° for a deposition done with a pulsed signal (0.2/0.8) to a continuous signal. Figures 11(c)–11(e) support Fig. 11(b) illustrating that carbon-containing groups at the surface of a deposited layer contribute to the hydrophobicity of the layer.[8]

Figure 12 shows the C1s spectra associated with the different films deposited with a varying DC. As the DC increases, an O–C=O component appears and increases, together with a decrease in intensity of the C–C, C–H component associated with the hydrophobic behavior. A broadening of the latter peak is also observed, especially toward higher binding energies, suggesting other components, possibly containing oxygen, and therefore more hydrophilic.

FIG. 12.

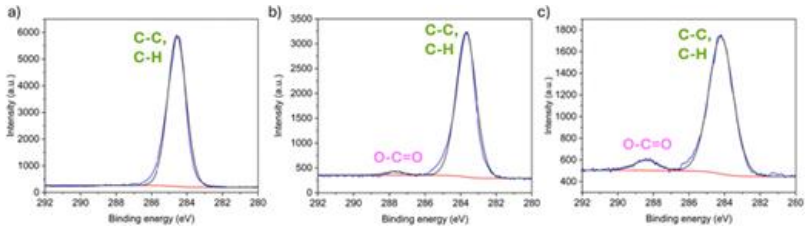

Surface (without etching) C1s XPS spectra of the different layers deposited with the different DBD modes: (a) DC = 20%, (b) DC = 50%, and (c) DC = 100%.

C. Deposition time

Whatever the deposition times, the layer resulted to be crystalline. For 5 and 10 min deposition times, the layer was not

crystalline enough exhibiting a small diffraction peak intensity and then small crystallinity [see Fig. 13(a)] for which crystal size cannot be calculated. With crystallinity increasing for 20 and 30 min deposition time, the calculated crystal sizes are comparable for crystallized layers (20 and 30 min). They are, respectively, 10.4 ± 0.05 and 12.84 ± 0.16 nm. In parallel, films deposited at short deposition times show a high carbon content, whereas at longer times, the carbon content is reduced [Fig. 13(b); measured by XPS]. This could be due to the heat applied to the substrate via the heating system which acts as a traditional annealing step in most of the deposition processes. Some researchers reported that carbon can diffuse out during annealing of the material[47] of the layer to purify the anatase film.

FIG. 13.

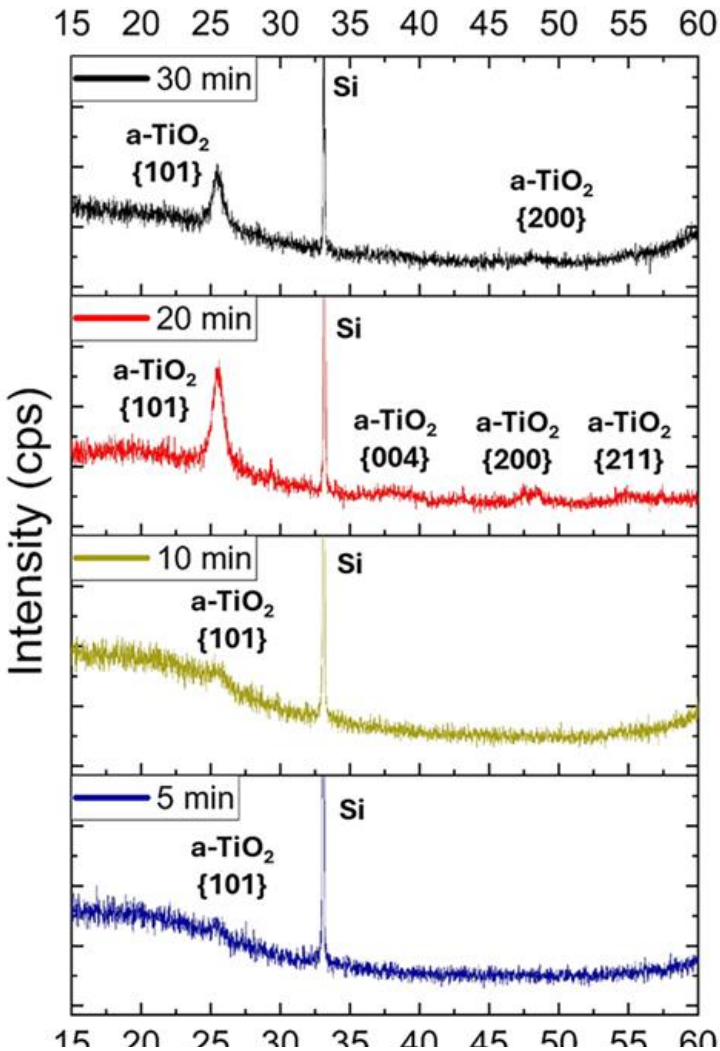

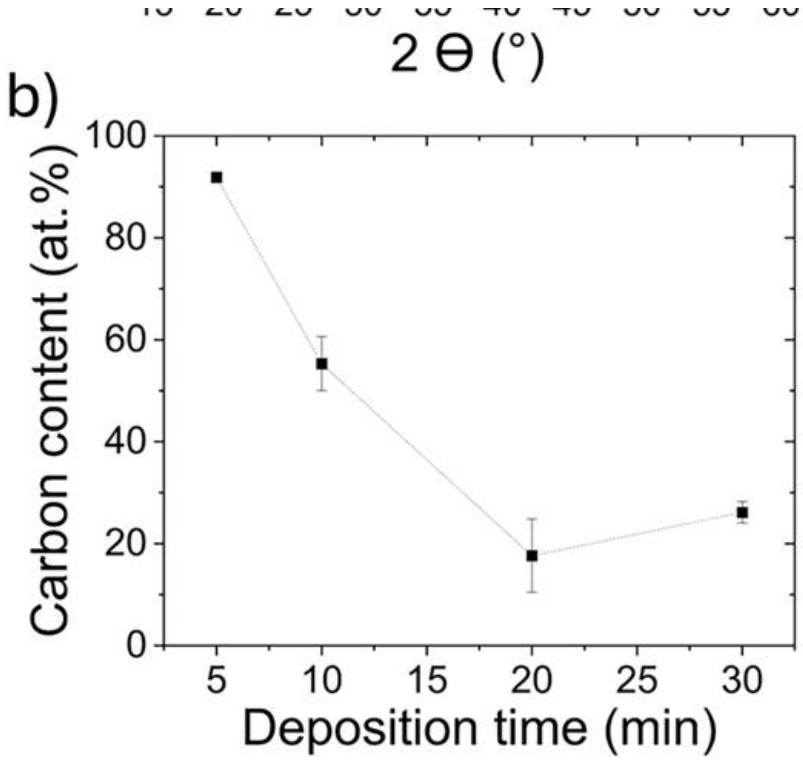

(a) XRD spectra of the different deposition time at a constant mean power of 45 W and a substrate temperature of 673 K, a bubbler temperature of 333 K, and Ar as a carrier gas. (b) Evolution of the carbon content (measured by XPS) with the deposition time, and dot line is used as a visual guide.

D. Bubbler temperature

Bubbler temperature directly drives the vapor pressure of TTIP and, therefore, the flow of TTIP into the plasma zone. This, in turn, influences the deposition rate and the overall kinetics of reaction and crystallization. Table IV summarizes the equivalence between the bubbler temperature, and the flow of liquid titanium precursor sent over a 1.5 slm (standard liter per minute) of Ar passing through the bubbler.

TABLE IV.

Summary of the correspondence between the bubbler temperature and the amount of liquid precursor vaporized with an Ar flow of 1.5 slm.

Bubbler temperature (K)	TTIP amount vaporized (mg/min; ±1 mg/min)

313	2.0
323	3.2
333	4.9
343	8.5
353	14.5
363	22.9

Figure 14(a) shows that an increase in the TTIP injection rate enhances the crystallinity of the deposited layers. This is evidenced by the observation that the main diffraction peak {101} at 25.4° keeps increasing with increasing TTIP flow. This could be due either to higher crystallinity of the layer (density) or more crystals that are diffracting (volume). In terms of crystal size, an increase in the fraction of TTIP injected in the discharge results in an increase in crystal size until a plateau is reached. However, at high TTIP flow rates (above 363 K), the depositions become powdery and no longer adhere to the substrate.

FIG. 14.

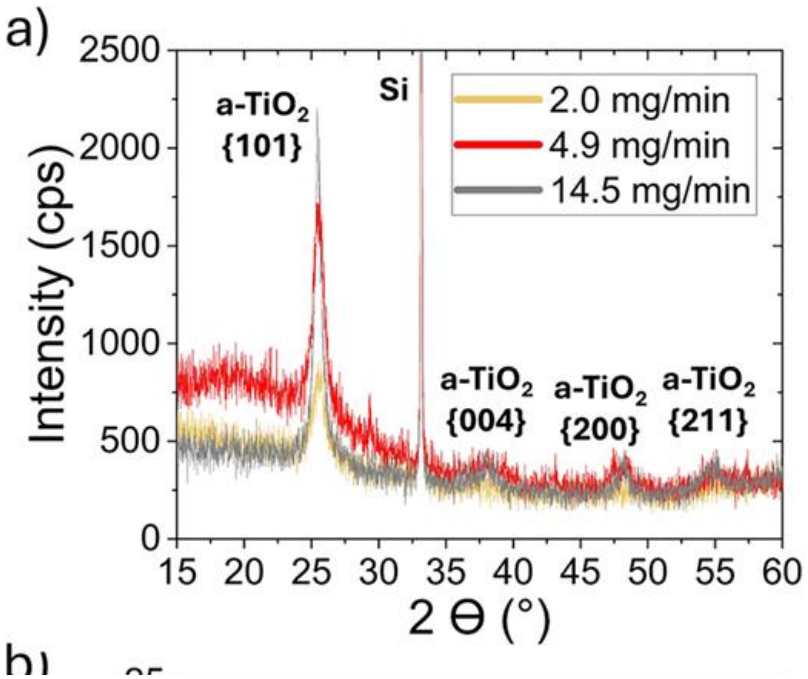

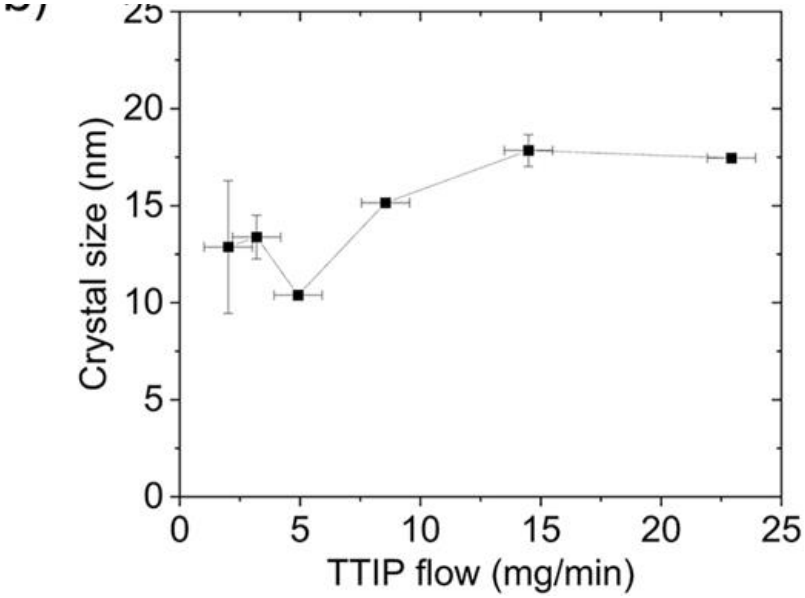

(a) Crystallinity study of the effect of TTIP flow argon as a carrier gas, a continuous 45 W of mean applied power, a substrate temperature of 673 K for 20 min. (b) Evolution of the crystal size with different precursor flowrates, and dot line is used as a visual guide.

E. Substrate temperature

Figure 15 shows the XRD spectra of the coatings deposited with substrate temperatures varying from 473 to 673 K. Most of the diffraction spectra present the typical {101} diffraction peak of anatase as well as small peaks for the other diffraction planes ({004}, {200}, and {211}) for the deposition carried out at 623 and 673 K, respectively. At lower substrate temperatures, a decrease in crystallinity is observed until the complete disappearance of crystallinity at 473 K. The coating deposited at 523 K with a small diffraction peak of the {101} plane represents the limit of crystallinity. This is in agreement with previous studies carried out at low pressure.[15,35] This work here shows that crystalline TiO_2 can be obtained at the same lowest temperature, but at atmospheric pressure. The average crystal size does not seem to depend on the substrate temperature (see Table V).

FIG. 15.

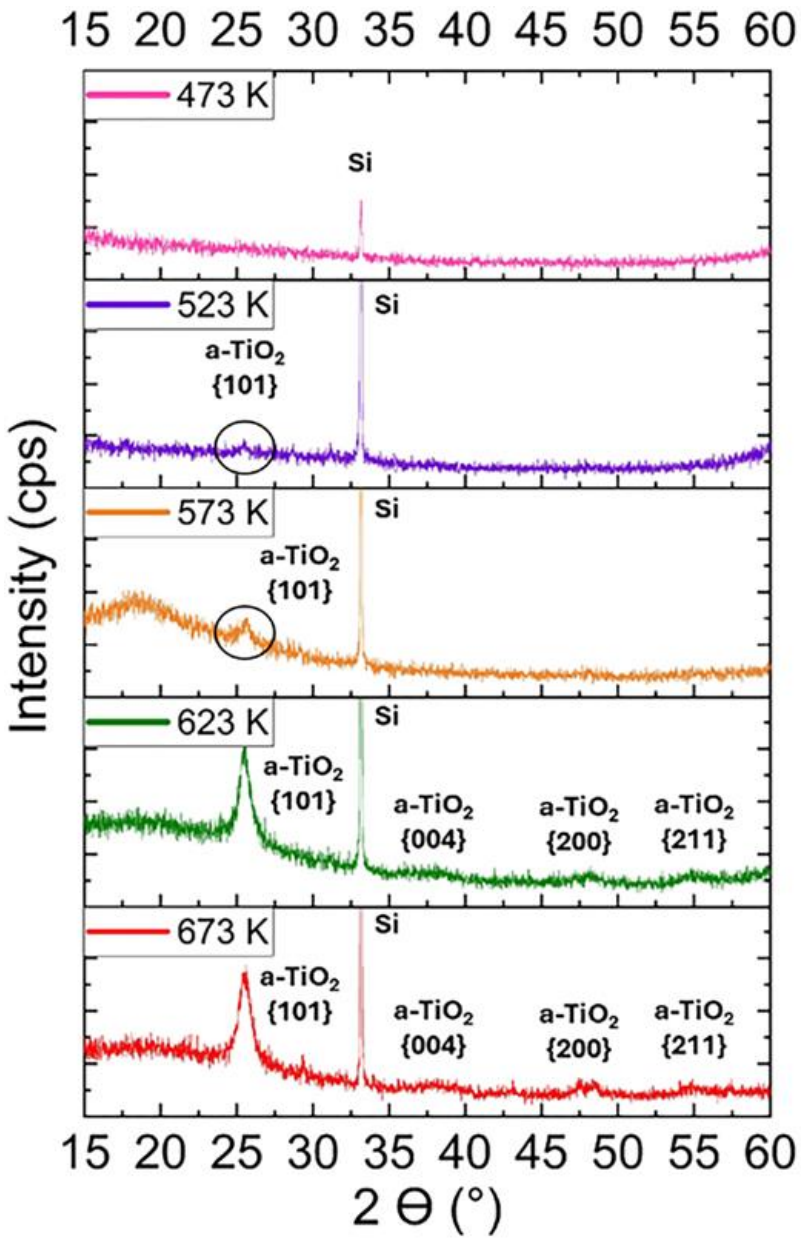

XRD spectra of depositions done at different substrate temperatures with a continuous mean applied power of 45 W, with Ar as a carrier gas, a bubbler temperature of 333 K, and 20 min as deposition time.

TABLE V.

Summary of the crystal size obtained with different substrate temperature.

Deposition temperature (K)	Crystal size (nm)
673	10.40 ± 0.05
623	11.76 ± 2.14

573	11.79 ± 0.32
523	Cannot be determined
473	Not crystalline

IV. CONCLUSIONS

This study demonstrates that a pure layer of TiO_2 anatase can be directly synthesized using an atmospheric pressure PECVD system coupled to an inductive heating system. The deposition parameters are shown to have a significant impact on film properties. For instance, the average crystal size is 12 nm when argon is used as a primary plasma gas, but it increases to 20 nm with nitrogen due to the lower ionization density. Pulsed power leads to an increase in surface carbon contamination due to the increased instantaneous power, resulting in hydrophobic coatings. Whatever the deposition time, a crystalline anatase layer could be synthesized. Only after 20 min of deposition time, the sufficient intensity of the diffraction signal could be obtained and to be able to estimate the mean crystal size which is of 12 ± 2 nm. Reducing the deposition time shows to go along with an increase in the carbon content which comes with a lower anneal-like time. A higher amount of TTIP injected into the system results in a larger crystal size because more reactant is injected into the reaction medium. Finally, crystalline anatase is deposited with a substrate temperature as low as 523 K (250 °C) at atmospheric pressure.

The next step of this research will focus on the comparison with other precursors and on increasing furthermore the average crystal size, at low temperature.

ACKNOWLEDGMENTS

This work is supported by the F.R.S.-FNRS PER (extraordinary

research project) “Virusurf” and the F.R.S.-FNRS “CrystallizaTiO_2(N)” project (N. Fosseur Ph.D. grant). The authors also thank the Jaumotte-Demoulin Foundation for financing the XPS analysis.

AUTHOR DECLARATIONS

Conflict of Interest

The authors have no conflicts to disclose.

Author Contributions

Nicolas Fosseur: Conceptualization (lead); Formal analysis (lead); Funding acquisition (equal); Investigation (lead); Methodology (lead); Writing – original draft (lead). **Thomas Fontaine:** Investigation (supporting); Methodology (supporting). **David Petitjean:** Resources (supporting). **Loïc Malet:** Formal analysis (supporting). **Rony Snyders:** Writing – review & editing (supporting). **Stéphane Godet:** Funding acquisition (equal); Supervision (equal); Validation (equal); Writing – review & editing (equal). **François Reniers:** Conceptualization (equal); Funding acquisition (equal); Project administration (lead); Supervision (equal); Validation (equal); Writing – review & editing (lead).

DATA AVAILABILITY

The data that support the findings of this study are available from the corresponding author upon reasonable request.

REFERENCES

1. Q. Junnan, L. Huimin, L. Guihong, and C. Yao, *Chem. Eng. J.* 491, 151773 (2024).
https://doi.org/10.1016/j.cej.2024.151773
Google Scholar Crossref

2. S. Huili, S. Chaoyun, L. Zhitong, Z. Long, W. Haifeng, and

2. S. Hafiz, S. Chaoyuan, J. Zhitong, Z. Long, W. Haifeng, and C. Jingbo, *RSC Adv.* 12, 33641 (2022).
https://doi.org/10.1039/D2RA05442F
Google Scholar Crossref PubMed

3. N. B. Saleh, A. Khalid, Y. Tian, C. Ayres, I. V. Sabaraya, J. Pietari, D. Hanigan, I. Chowdhury, and O. G. Apul, *Environ. Sci.: Water Res. Technol.* 5, 198 (2019).
https://doi.org/10.1039/C8EW00621K
Google Scholar Crossref

4. S. Almaie, V. Vatanpour, M. H. Rasoulifard, and I. Koyuncu, *Chemosphere* 306, 135655 (2022).
https://doi.org/10.1016/j.chemosphere.2022.135655
Google Scholar Crossref PubMed

5. W. A. Thompson, C. Perier, and M. M. Maroto-Valer, *Appl. Catal., B* 238, 136 (2018).
https://doi.org/10.1016/j.apcatb.2018.07.018
Google Scholar Crossref

6. M. Rafique, S. Hajra, M. Irshad, M. Usman, M. Imran, M. A. Assiri, and W. M. Ashraf, *ACS Omega* 8, 25640 (2023).
https://doi.org/10.1021/acsomega.3c00963
Google Scholar Crossref PubMed

7. D. Wang, Q. Yang, Y. Guo, X. Liu, J. Shi, and J. Zhang, *Mater. Lett.* 65, 2526 (2011).
https://doi.org/10.1016/j.matlet.2011.05.054
Google Scholar Crossref

8. J. Kyte, *Biophys. Chem.* 100, 193 (2002).
https://doi.org/10.1016/S0301-4622(02)00281-8
Google Scholar Crossref

9. Z. F. Yin, L. Wu, H. G. Yang, and Y. H. Su, *Phys. Chem. Chem. Phys.* 15, 4844 (2013).
https://doi.org/10.1039/c3cp43938k
Google Scholar Crossref PubMed

10. Y. Ohko, S. Saitoh, T. Tatsuma, and A. Fujishima, *J. Electrochem. Soc.* 148, B24 (2001).
https://doi.org/10.1149/1.1339030
Google Scholar Crossref

11. S. Obregón and V. Rodríguez-González, *J. Sol-Gel Sci. Technol.* 102, 125 (2022).
https://doi.org/10.1007/s10971-021-05628-5
Google Scholar Crossref

12. J. Yu, J. C. Yu, M. K.-P. Leung, W. Ho, B. Cheng, X. Zhao, and J. Zhao, *J. Catal.* 217, 69 (2003).
https://doi.org/10.1016/S0021-9517(03)00034-4
Google Scholar Crossref

13. S. Mahsid, M. Askari, and M. Sasani Ghamsari, *J. Mater. Process. Technol.* 189, 296300 (2007).
https://doi.org/10.1016/j.jmatprotec.2007.01040
Google Scholar

14. Y. M. Abdulraheem, S. Ghoraishi, L. Arockia-Thai, S. K. Zachariah, and M. Ghannam, *Adv. Mater. Sci. Eng.* 2013, 1 (2013). https://doi.org/10.1155/2013/574738
Google Scholar Crossref

15. A. Borras, J. R. Sanchez-Valencia, R. Wildmer, V. J. Rico, A. Justo, and A. R. Gonzalez-Elipe, *Cryst. Growth Des.* 9, 2868 (2009). https://doi.org/10.1021/cg9001779
Google Scholar Crossref

16. G. A. Battiston, R. Gerbasi, A. Gregori, M. Porchia, S. Cattarin, and G. A. Rizzi, *Thin Solid Films* 371, 126 (2000).
https://doi.org/10.1016/S0040-6090(00)00998-6
Google Scholar Crossref

17. M. Hans, J. M. Schneider, A. Matthews, and C. Mitterer, *Surf. Coat. Technol.* 494, 131486 (2024).
https://doi.org/10.1016/j.surfcoat.2024.131486
Google Scholar Crossref

18. D. Merche, N. Vandecasteele, and F. Reniers, *Thin Solid Films* 520, 4219 (2012).
https://doi.org/10.1016/j.tsf.2012.01.026
Google Scholar Crossref

19. Y. Xu, Y. Zhang, L. Li, K. Ding, Y. Guo, J. Shi, X. Huang, and J. Zhang, *Plasma Chem. Plasma P.* 39, 937947 (2019).
https://doi.org/10.1007/s11090-019-09961-0
Google Scholar Crossref

20. S. Banerjee, E. Adhikari, P. Sapkota, A. Sebastian, and S. Ptasinska, *Materials* 13, 2931 (2020).
https://doi.org/10.3390/ma13132931
Google Scholar Crossref PubMed

21. S. Collette et al, *Surf. Coat. Technol.* 289, 172 (2016).
https://doi.org/10.1016/j.surfcoat.2016.01.049
Google Scholar Crossref

22. K. Baba, S. Bulou, P. Choquet, and N. D. Boscher, *ACS Appl. Mater. Interfaces* 9, 13733 (2017).
https://doi.org/10.1021/acsami.7b01398
Google Scholar Crossref PubMed

23. T. Homola, P. Dzik, M. Vesely, J. Kelar, M. Cernak, and M. Weiter, *ACS Appl. Mater. Interfaces* 8, 33562 (2016).
https://doi.org/10.1021/acsami.6b09556
Google Scholar Crossref PubMed

24. Y. Gazal, C. Chazelas, C. Dublanche-Tixier, and P. Tristant, *J. Appl. Phys.* 121, 123301 (2017).
https://doi.org/10.1063/1.4979024
Google Scholar Crossref

25. A. Perraudeau, C. Dublanche-Tixier, P. Tristant, and C. Chazelas, *Appl. Surf. Sci.* 493, 703 (2019).
https://doi.org/10.1016/j.apsusc.2019.07.057
Google Scholar Crossref

26. K. Navaneetha Pandiyaraj et al, *Surf. Coat. Technol.* 389, 125642 (2020).
https://doi.org/10.1016/j.surfcoat.2020.125642
Google Scholar Crossref

27. Q. Chen, Q. Liu, J. Hubert, W. Huang, K. Baert, G. Wallaert, H. Terryn, M.-P. Delplancke-Ogletree, and F. Reniers, *Surf. Coat. Technol.* 310, 173 (2017).
https://doi.org/10.1016/j.surfcoat.2016.12.077
Google Scholar Crossref

28. Q. Chen et al, *Thin Solid Films* 664, 90 (2018).
https://doi.org/10.1016/j.tsf.2018.08.025
Google Scholar Crossref

29. A. Chauvin, C. Bittencourt, M. Galais, L. Sauvage, M. Bellefroid, C. Van Lint, A. Op de Beeck, R. Snyders, and F. Reniers, *Surf. Coat. Technol.* 472, 129936 (2023).
https://doi.org/10.1016/j.surfcoat.2023.129936
Google Scholar Crossref

30. A. Remy, M. Serigne Fall, T. Segato, S. Godet, M.-P. Delplancke-Ogletree, P. Panini, Y. Eerts, and F. Reniers, *Thin Solid Films* 688, 137437 (2019).
https://doi.org/10.1016/j.tsf.2019.137437
Google Scholar Crossref

31. M. Brabant et al, *Surf. Coat. Technol.* 495, 131559 (2025). https://doi.org/10.1016/j.surfcoat.2024.131559
Google Scholar Crossref

32. M. Brabant, A. Demaude, J. Zveny, A. Remy, T. Segato, D. Petitjean, M.-P. Delplancke-Ogletree, and F. Reniers, *J. Vac. Sci. Technol. A* 42, 023008 (2024).
https://doi.org/10.1116/6.0003268
Google Scholar Crossref

33. X. Wang et al, *J. Catal.* 310, 100 (2014).
https://doi.org/10.1016/j.jcat.2013.04.022
Google Scholar Crossref

34. J. Zhang, P. Zhou, J. Liu, and J. Yu, *Phys. Chem. Chem. Phys.* 16, 20382 (2014).
https://doi.org/10.1039/C4CP02201G
Google Scholar Crossref PubMed

35. L. Youssef, A. J. Kinfack Leoga, S. Roualdes, J. Bassil, M. Zakhour, V. Rouessac, A. Ayral, and M. Nakhl, *J. Eur. Ceram. Soc.* 37, 5289 (2017).
https://doi.org/10.1016/j.jeurceramsoc.2017.05.010
Google Scholar Crossref

36. W. Yang and C. A. Wolden, *Thin Solid Films* 515, 1708 (2006). https://doi.org/10.1016/j.tsf.2006.06.010
Google Scholar Crossref

37. A. Borrás, J. Cotrino, and A. R. González-Elipe, *J. Electrochem. Soc.* 154, P152 (2007).
https://doi.org/10.1149/1.2794289

Google Scholar Crossref

38. A. Remy and F. Reniers, E.U. patent N EP3768048A1 (19 July 2019).

39. J. Wei, A. Ostadhossein, S. Li, and M. Ihme, *Proc. Combust. Inst.* 38, 1433 (2021). https://doi.org/10.1016/j.proci.2020.06.345
Google Scholar Crossref

40. P. Buerger, D. Nurkowski, J. Akroyd, and M. Kraft, *Proc. Combust. Inst.* 36, 1019 (2017). https://doi.org/10.1016/j.proci.2016.08.062
Google Scholar Crossref

41. J. Voráč, P. Synek, V. Procházka, and T. Hoder, *J. Phys. D: Appl. Phys.* 50, 294002 (2017). https://doi.org/10.1088/1361-6463/aa7570
Google Scholar Crossref

42. E. H. Bjarnason, B. Omarsson, S. Engmann, F. H. Omarsson, and O. Ingolfsson, *Eur. Phys. J. D* 68, 121 (2014). https://doi.org/10.1140/epjd/e2014-50091-9
Google Scholar Crossref

43. Y.-C. Kim, H.-C. Lee, Y.-S. Kim, and C.-W. Chung, *Phys. Plasmas* 22, 083512 (2015). https://doi.org/10.1063/1.4928907
Google Scholar Crossref

44. N. Britun, M. Gaillard, A. Ricard, Y. M. Kim, K. S. Kim, and J. G. Han, *J. Phys. D: Appl. Phys.* 40, 1022 (2007). https://doi.org/10.1088/0022-3727/40/4/016
Google Scholar Crossref

45. A. Amini, M. S. Zakerhamidi, and S. Khorram, *Physica B* 612, 412820 (2021). https://doi.org/10.1016/j.physb.2021.412820
Google Scholar Crossref

46. S. Mathur and P. Kuhn, *Surf. Coat. Technol.* 201, 807 (2006). https://doi.org/10.1016/j.surfcoat.2005.12.039
Google Scholar Crossref

47. D. G. Piliptsou, X. H. Jiang, A. S. Chaus, A. V.

Rogachev, and L. Morovic, *Diamond Relat. Mater.* 135, 109890 (2023).
https://doi.org/10.1016/j.diamond.2023.109890
Google Scholar Crossref